Editors' Suggestion

IrO_2 Surface Complexions Identified through Machine Learning and Surface Investigations

Jakob Timmermann,[1] Florian Kraushofer,[2] Nikolaus Resch,[2] Peigang Li,[3] Yu Wang,[4] Zhiqiang Mao,[3,4] Michele Riva,[2] Yonghyuk Lee,[1] Carsten Staacke,[1] Michael Schmid,[2] Christoph Scheurer,[1] Gareth S. Parkinson,[2] Ulrike Diebold,[2] and Karsten Reuter[1,5,*]

[1]*Chair for Theoretical Chemistry and Catalysis Research Center, Technical University of Munich, Lichtenbergstrasse 4, D-85747 Garching, Germany*

[2]*Institute of Applied Physics, Technical University of Vienna, Wiedner Hauptstrasse 8-10/134, A-1040 Vienna, Austria*

[3]*Department of Physics and Engineering Physics, Tulane University, New Orleans, Louisiana 70118, USA*

[4]*Department of Physics, The Pennsylvania State University, University Park, Pennsylvania 16802, USA*

[5]*Fritz-Haber-Institut der Max-Planck-Gesellschaft, Faradayweg 4-6, D-14195 Berlin, Germany*

(Received 5 July 2020; accepted 22 September 2020; published 10 November 2020)

A Gaussian approximation potential was trained using density-functional theory data to enable a global geometry optimization of low-index rutile IrO_2 facets through simulated annealing. *Ab initio* thermodynamics identifies (101) and (111) (1×1) terminations competitive with (110) in reducing environments. Experiments on single crystals find that (101) facets dominate and exhibit the theoretically predicted (1×1) periodicity and x-ray photoelectron spectroscopy core-level shifts. The obtained structures are analogous to the complexions discussed in the context of ceramic battery materials.

DOI: 10.1103/PhysRevLett.125.206101

First-principles computations based on density-functional theory (DFT) have become a standard tool to determine surface structure. In the standard approach, a set of trial structures are optimized geometrically to identify minima on the ground-state potential-energy surface. Observables are computed to check for consistency with experimental data, and one structure is declared best. While successful, this approach depends on the trial structures, and it is possible that the true surface is simply missed.

With the increasing efficiency of DFT calculations and computational power, DFT-based, global geometry optimization has been heralded as a significant step to overcome this limitation [1–6]. Despite impressive successes of simulated annealing or basin hopping work, this direct approach has never truly affected the popularity of the "trial set and local geometry optimization" approach. The excessive number of computations required by even the most efficient algorithms [7,8] leads to an intractable computational demand, particularly for reconstructions with large surface unit cells. Fortunately, machine-learned (ML) interatomic potentials [9,10] may now overcome this deadlock, and enable a paradigm shift in our approach to automatic structure searches. These potentials can be trained with a feasible number of DFT calculations and, if needed, can be retrained on the fly in the course of an ongoing global geometry optimization. Crucially, the optimization is performed using the inexpensive ML potential, which enables extensive sampling of the configuration space.

Here, we use this approach to find the most stable surface terminations of rutile-structured oxides. Our motivation came from empirical reports that IrO_2 catalysts for proton-exchange membrane water electrolysis exhibit increased activity following electrochemical activation with a small number of reductive formation cycles [11,12]. We hypothesized this might originate in a metal-rich complexion, which is similar to the complexions discussed in the context of ceramic battery materials [13]. A complexion is a surface (or interfacial) phase that possesses a thermodynamically determined equilibrium thickness on the order of nanometers, but is neither a thin version of a known 3D bulk phase nor merely a reconstructed surface layer. While the ubiquity and importance of complex (often large surface-unit-cell) reconstructions at surfaces of compound catalysts under operation conditions is well known [14–18], complexions can be more subtle by only involving deeper compositional changes at unchanged translational symmetry. After training a ML Gaussian approximation potential (GAP) [19,20] with DFT data, simulated-annealing-based global optimization immediately leads to very stable new terminations on the (101) and (111) low-index surfaces of rutile IrO_2 with mixed Ir—Ir and Ir—O bonding. Direct *ab initio* thermodynamics [21] calculations confirm the high stability of these complexions under strongly reducing conditions [22]—not only on IrO_2, but also on RuO_2, which is the alternative state-of-the-art rutile-structured catalyst used in proton-exchange membrane electrolysis. The theoretical predictions are supported by surface investigations of IrO_2 single crystals, which exhibit (101) facets rather than the more common low-energy (110) orientation of rutile [23,24]. Characterization by low-energy

electron diffraction (LEED), scanning-tunneling microscopy (STM), and x-ray photoelectron spectroscopy (XPS) confirms the properties of the predicted metal-rich complexions, explaining why IrO_2 nanoparticles often expose (101) facets [25–31].

Our investigation starts with the creation of a reference database of DFT structures to train the nonparametric GAP potential. GAPs decompose the total energy of a system into a sum of atomic energies that depend on the local chemical environment [19,20]. This dependence is learned from the atomic environments present in the reference database through Gaussian process regression. For energy predictions, the similarity between each atom in an unknown structure and representative training atoms is then determined via a kernel function. In this work, we employ the smooth overlap of atomic positions kernel [32], which considers all neighboring atoms within a radius of 5.5 Å, combined with a simple two-body kernel based on interatomic distances. The reference database comprises 136 structures calculated with QUANTUMESPRESSO [33] and the revised Perdew-Burke-Ernzerhof (RPBE) [34] exchange-correlation functional. These structures span a range of most diverse chemical environments, and comprise various optimized or near-optimum crystalline bulk and low-index surface geometries of different stoichiometry, as well as highly nonequilibrium structures taken from snapshots of high-temperature molecular dynamics (MD) simulations of differently shaped and sized nanoparticles. Validated against an equally diverse set of 39 structures not used in the training, the final GAP reproduces the widely varying DFT formation energies with a mean average error of 25 meV/atom.

To explore a possible formation of complexions, we performed extensive simulated-annealing MD runs for all five symmetry-inequivalent low-index surfaces [35] of rutile IrO_2, each time starting with the metal-rich regular (1×1) termination expected under reducing conditions. Specifically, we employ periodic boundary-condition supercells with thick slabs comprising at least seven rutile trilayers and (3×3) or (4×4) surface unit cells as further detailed in the Supplemental Material (SM) [36]. The temperature is initially raised to around 1000 K for 20 ps, before a slow cooling rate of 3 K/ps is applied during an additional 250 ps. After a final geometry optimization, we obtain new structures with a significantly lower energy, in particular for the (101) [or the symmetry equivalent (011)] and the (111) orientations. Analysis of these structures (Fig. 1) reveals that neither correspond to a reconstruction with a lowered translational symmetry, but is instead a reordering of the original rutile layering sequence that preserves the regular (1×1) lateral periodicity. Direct recalculation and geometry reoptimization of these structures at the DFT-RPBE level confirms the reliability of the GAP prediction. The structures are significantly lower in energy than the regular Ir-rich (1×1) termination for the respective orientation and, in slabs where at least the five topmost layers are allowed to move, the regular Ir-rich (101) termination relaxes barrierlessly into the new complexion.

Within an *ab-initio* thermodynamics framework [21], we can compare the stability of these new structures to all other possible and known (1×1) terminations of rutile IrO_2. Generally, there is at least one metal-rich, one stoichiometric, and one oxygen-rich termination for each low-index facet, with some facets lacking some terminations and some facets additionally allowing for an oxygen-superrich termination (Figs. S7–S11 of SM [36]) [44]. Figure 1 shows the resulting surface phase diagram. Only the lowest surface free energy is shown for each facet as a function of the chemical potential of oxygen $\Delta\mu_O$, and a kink in the

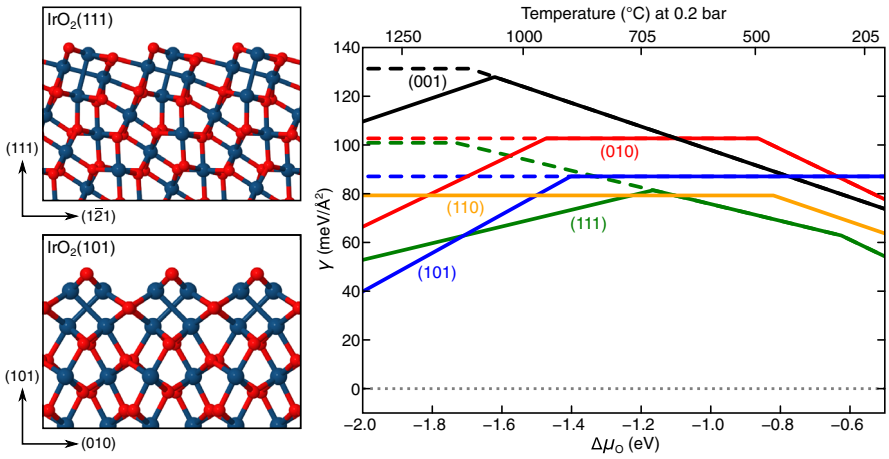

FIG. 1. Left: side views of identified complexions. Ir and O atoms are drawn as blue (large) and red (small) spheres, respectively. Right: computed surface free energies γ of the five symmetry-inequivalent low-index facets in a pure oxygen atmosphere. In the top x axis, the dependence on the oxygen chemical potential $\Delta\mu_O$ is translated into a temperature scale at 0.2 bar pressure (the oxygen partial pressure in air). The dashed lines indicate the surface free energies without complexions.

surface free-energy line reflects a change in the most stable termination. Metal-rich terminations exhibit a positive slope, O-rich terminations a negative slope, and stoichiometric terminations are independent of $\Delta\mu_O$. For low oxygen chemical potentials, the complexions significantly lower the surface free energy and change the relative energetic ordering. The same form and relative ordering of the surface free energies is obtained with the stronger-binding Perdew-Burke-Ernzerhof (PBE) [45] functional, but the entire phase diagram shifts to lower $\Delta\mu_O$ (see Fig. S13 of SM [36]). While we cannot quantify the gas-phase conditions of the phase stability, the (110) facet would clearly be the lowest-energy orientation in reducing environments in the absence of complexations, in line with the predominant focus of surface-science work on this particular facet [23,24]. The stability of the complexions makes the (101) and (111) facets energetically competitive.

In order to test this surprising finding, we investigate the surfaces of IrO_2 single crystals grown in a tube furnace with an O_2 inflow of 100 ml/min at atmospheric pressure. Ir was supplied from Ir powder (Alfa Aesar, 99.99%) at 1250 °C, and flake-shaped IrO_2 crystals formed at the colder end of the furnace (1000 °C). Two of the larger crystallites (both ca. 3 mm^2 top surface area) were chosen for surface studies. Electron backscatter diffraction immediately reveals that all areas where a diffraction pattern could be identified expose (101)-type surfaces (Fig. S18 of SM [36]).

The two IrO_2 samples were then loaded to an ultrahigh vacuum (UHV) chamber and prepared by sputtering (1 keV Ar^+ ions, $p_{Ar} = 8 \times 10^{-6}$ mbar, 10 min) and annealing in oxygen (450 °C, 40 min). Oxygen gas was dosed through an oxygen shower, with the gas outlet very close to the sample. This increases the local pressure by a factor of 10–30 compared to the O_2 pressure measured in the chamber (5×10^{-6} mbar).

Low-energy electron diffraction (LEED) images [Fig. 2(b) herein, and Fig. S20 in the SM [36]] reveal a rectangular pattern with the spots moving toward the center of the screen with increasing incident beam energy. The unit cell size of $(0.58 \pm 0.04) \times (0.47 \pm 0.04)$ nm^2 was quantified using LEED patterns of a Pd(111) single crystal as a reference. These numbers are in good agreement with the (1×1) unit cell of $IrO_2(101)$ (0.55×0.45 nm^2). Some additional diffraction spots are also observed, but these move in nonradial directions with increasing energy, indicating the presence of other facets for which the beam incidence is off normal.

STM images acquired at room temperature after UHV preparation [Fig. 2(a)] exhibit a zigzag pattern with (1×1) periodicity. Since the intrinsic drift of the STM scanner cannot be corrected by comparison to a known structure, distance measurements are unreliable, but the 0.55×0.45 nm^2 spacing expected for an $IrO_2(101)$-(1×1) unit cell fits the data within the expected error. Some bright

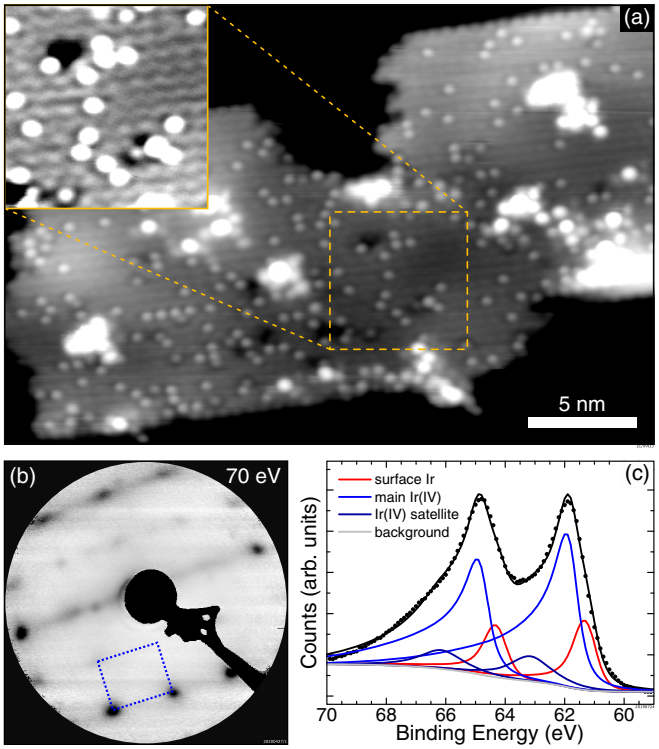

FIG. 2. IrO_2 crystal after UHV preparation. (a) STM image of the IrO_2 sample (30×20 nm^2, $U_{sample} = -2$ V, $I_{tunnel} = 0.2$ nA) with the inset processed to enhance the visibility of the atomic corrugation. (b) LEED pattern from one of the IrO_2 crystals ($E_{electron} = 70$ eV). A rectangular pattern (unit cell drawn in blue) is clearly visible, and its diffraction spots move toward the center of the screen with increasing energy, as expected for normal beam incidence. (c) XPS data (points) and fit (lines) of the Ir $4f$ region (Mg Kα anode).

point features are also visible, which we attribute to either lattice defects or adsorbates. Interestingly, the periodicity of these protrusions cannot be reconciled with a bulk-truncated (1×1) surface (Fig. S22 [36]). On the proposed complexion, the features are located at surface oxygen sites, allowing tentative assignment as either surface hydroxyls or oxygen vacancies.

On one of the samples, a second, pseudohexagonal surface phase was also observed (Fig. S19 [36]). The nearest-neighbor distances were determined as ≈0.55 nm, which would fit an $IrO_2(111)$-(1×1) unit cell. However, since the unit-cell angle cannot be accurately determined by STM alone, a (2×2) superstructure on Ir(111) could, in principle, also fit the data. We also note that a hexagonal reconstruction of the (101) facet was previously observed on rutile $TiO_2(101)$ [46] and attributed to contamination.

XPS of the Ir $4f$ region is shown in Fig. 2(c). We fit the spectrum using peak shapes and oxide satellite peak positions from Ref. [47], which results in a peak at 61.9 eV (blue) due to Ir(IV) and a lower-binding-energy component shifted by 0.6 eV at 61.3 eV (red). This agrees with our initial-state calculations of the $4f$ DFT

Kohn-Sham orbital positions for the $IrO_2(101)$ complexion, which yield an initial-state shift of 0.6 eV for the top two Ir layers with respect to a bulklike Ir atom deeper in the IrO_2 slab using both the RPBE and PBE functionals (see SM [36]). A much larger shift (1.1 eV toward lower binding energies) is predicted for the top layer of the regular Ir-rich (101) termination. We also acquired Ir $4f$ XPS peaks from a freshly sputtered sample (Fig. S21 [36]), which is dominated by a strong contribution of metallic surface iridium at 60.9 eV, in agreement with the position reported in the literature for Ir single crystals [32]. Overall, the experimental evidence clearly shows that the crystals are dominated by (101) facets with a (1×1) surface symmetry, and supports the predicted $IrO_2(101)$-(1×1) complexion. Since the crystal growth direction was not enforced, and the relatively rough, vicinal surfaces would have faceted to a more stable orientation, the dominance of the (101) surface is an indirect confirmation of its thermodynamic stability at the growth conditions.

In our view, the complexions are precursors to a full reduction of the bulk oxide. Two layers with mixed Ir—O and Ir—Ir bonding are obtained through a mere reordering of the rutile layering sequence of the (101) and (111) orientations. The increased coordination of the topmost Ir atoms (from threefold to fourfold) stabilizes the structures. Adding further equivalent complexion layers does not further increase this coordination, and we calculate higher surface free energies for such structures (see Fig. S12 [36]). As such, the identified complexions are novel 2D interphases, and not just thin versions of known 3D bulk structures. They are thus quite analogous to the much discussed surface oxides as precursors to a full oxidation of transition metals [48–50].

With this understanding, one would expect complexions to be a general feature of oxides in reducing environments, and follow-up computations predict that analogous complexions render the (101) and (111) facets energetically competitive for rutile RuO_2 under reducing conditions (Fig. S14 [36]).

In summary, a completely unexpected class of surface structures was readily identified for a well-studied type of oxide crystals using ML interatomic potentials. That such simple structures have consistently eluded previous trial-structure-based surface structure determination work on IrO_2 or RuO_2 shows them to be counterintuitive, and one wonders how many more surprises await us when global geometry optimization based on predictive-quality machine-learned potentials has reached full maturity.

See Supplemental Material [36] for additional detailed information on the reference database employed for the training of the ML potential and simulated-annealing runs, on the *ab initio* thermodynamics results, on the initial-state core level-shift calculations, as well as on the experimental growth and characterization work.

All input and output files for the DFT training structures are available at the NOMAD database [51].

This research was supported by the Kopernikus/P2X programme (Cluster FC-A1) of the German Federal Ministry of Education and Research, the German Federal Environmental Foundation DBU, and the German Academic Exchange Service DAAD. U. D., M. R., and F. K. acknowledge support by the Austrian Science Fund (FWF, Z-250, Wittgenstein Prize). G. S. P. acknowledges funding from the European Research Council (ERC) under the European Union's Horizon 2020 research and innovation program Grant Agreement No. 864628. N. R. was supported by the Austrian Science Fund (FWF, Y847-N20, START Prize). Z. M. acknowledges the support from the U.S. National Science Foundation under Grant No. DMR 1917579. We acknowledge fruitful discussions with Johannes Margraf and Simon Wengert. The authors thank Andreas Steiger-Thirsfeld (Universitäre Service-Einrichtung für Transmissions-Elektronenmikroskopie, TU Wien) for support with SEM measurements.

*Corresponding author.
karsten.reuter@ch.tum.de

[1] G. Kresse, W. Bergermayer, R. Podloucky, E. Lundgren, R. Koller, M. Schmid, and P. Varga, Complex surface reconstructions solved by *ab initio* molecular dynamics, Appl. Phys. A **76**, 701 (2003).

[2] H. A. Hussein, J. B. A. Davis, and R. L. Johnston, DFT global optimisation of gas-phase and MgO-supported subnanometre AuPd clusters, Phys. Chem. Chem. Phys. **18**, 26133 (2016).

[3] C. Panosetti, K. Krautgasser, D. Palagin, K. Reuter, and R. J. Maurer, Global materials structure search with chemically motivated coordinates, Nano Lett. **15**, 8044 (2015).

[4] L. B. Vilhelmsen and B. Hammer, A genetic algorithm for first principles global structure optimization of supported nano structures, J. Chem. Phys. **141**, 044711 (2014).

[5] R. B. Wexler, T. Qiu, and A. M. Rappe, Automatic prediction of surface phase diagrams using *ab initio* grand canonical Monte Carlo, J. Phys. Chem. C **123**, 2321 (2019).

[6] Y. Zhou, M. Scheffler, and L. M. Ghiringhelli, Determining surface phase diagrams including anharmonic effects, Phys. Rev. B **100**, 174106 (2019).

[7] D. J. Wales, J. P. K. Doye, M. A. Miller, P. N. Mortenson, and T. R. Walsh, Energy landscapes: From clusters to biomolecules, in *Advances in Chemical Physics*, edited by I. Prigogine and S. A. Rice (Wiley, 2000), Vol. 115, https://doi.org/10.1002/9780470141748.ch1.

[8] J. D. Pintér, *Global Optimization: Scientific and Engineering Case Studies*, Nonconvex Optimization and Its Applications, Vol. 85 (Springer, New York, 2006).

[9] M. Rupp, O. A. von Lilienfeld, and K. Burke, Guest editorial: special topic on data-enabled theoretical chemistry, J. Chem. Phys. **148**, 241401 (2018).

[10] J. Behler, Perspective: Machine learning potentials for atomistic simulations, J. Chem. Phys. **145**, 170901 (2016).

[11] A. Weiß, A. Siebel, M. Bernt, T.-H. Shen, V. Tileli, and H. A. Gasteiger, Impact of intermittent operation on lifetime and performance of a PEM water electrolyzer, J. Electrochem. Soc. **166**, F487 (2019).
[12] T. Reier, D. Teschner, T. Lunkenbein, A. Bergmann, S. Selve, R. Kraehnert, R. Schlögl, and P. Strasser, Electrocatalytic oxygen evolution on iridium oxide: Uncovering catalyst-substrate interactions and active iridium oxide species, J. Electrochem. Soc. **161**, F876 (2014).
[13] J. Luo, Let thermodynamics do the interfacial engineering of batteries and solid electrolytes, Energy Storage Mater. **21**, 50 (2019).
[14] J. M. P. Martirez, S. Kim, E. H. Morales, B. T. Diroll, M. Cargnello, T. R. Gordon, C. B. Murray, D. A. Bonnell, and A. M. Rappe, Synergistic oxygen evolving activity of a TiO_2-rich reconstructed $SrTiO_3(001)$ surface, J. Am. Chem. Soc. **137**, 2939 (2015).
[15] X. Rong and A. M. Kolpak, Ab initio approach for prediction of oxide surface structure, stoichiometry, and electrocatalytic activity in aqueous solution, J. Phys. Chem. Lett. **6**, 1785 (2015).
[16] A. B. Laursen *et al.*, Climbing the volcano of electrocatalytic activity while avoiding catalyst corrosion: Ni_3P, a hydrogen evolution electrocatalyst stable in both acid and alkali, ACS Catal. **8**, 4408 (2018).
[17] R. B. Wexler, J. M. P. Martirez, and A. M. Rappe, Active role of phosphorus in the hydrogen evolving activity of nickel phosphide (0001) surfaces, ACS Catal. **7**, 7718 (2017).
[18] M. Riva, M. Kubicek, X. Hao, G. Franceschi, S. Gerhold, M. Schmid, H. Hutter, J. Fleig, C. Franchini, B. Yildiz, and U. Diebold, Influence of surface atomic structure demonstrated on oxygen incorporation mechanism at a model perovskite oxide, Nat. Commun. **9**, 1 (2018).
[19] A. P. Bartók, M. C. Payne, R. Kondor, and G. Csányi, Gaussian Approximation Potentials: The Accuracy of Quantum Mechanics, without the Electrons, Phys. Rev. Lett. **104**, 136403 (2010).
[20] V. L. Deringer, M. A. Caro, and G. Csányi, Machine learning interatomic potentials as emerging tools for materials science, Adv. Mater. **31**, 1902765 (2019).
[21] K. Reuter, *Ab initio* thermodynamics and first-principles microkinetics for surface catalysis, Catal. Lett. **146**, 541 (2016).
[22] C. L. McDaniel and S. J. Schneider, Phase relations in the Ru-Ir-O_2 system in air, J. Res. Natl. Bur. Stand., Sect. A **73A**, 213 (1969).
[23] Z. Liang, T. Li, M. Kim, A. Asthagiri, and J. F. Weaver, Low-temperature activation of methane on the $IrO_2(110)$ surface, Science **356**, 299 (2017).
[24] M. J. S. Abb, T. Weber, L. Glatthaar, and H. Over, Growth of ultrathin single-crystalline $IrO_2(110)$ films on a $TiO_2(110)$ single crystal, Langmuir **35**, 7720 (2019).
[25] Y. Lee, J. Suntivich, K. J. May, E. E. Perry, and Y. Shao-Horn, Synthesis and activities of rutile IrO_2 and RuO_2 nanoparticles for oxygen evolution in acid and alkaline solutions, J. Phys. Chem. Lett. **3**, 399 (2012).
[26] X. Zeng, D. Dang, L. Leng, C. You, G. Wang, C. Zhu, and S. Liao, Doped reduced graphene oxide mounted with IrO_2 nanoparticles shows significantly enhanced performance as a cathode catalyst for Li-O_2 batteries, Electrochim. Acta **192**, 431 (2016).
[27] C. Felix, J. B. Bladergroen, V. Linkov, G. B. Pollet, and S. Pasupathi, *Ex-situ* electrochemical characterization of IrO_2 synthesized by a modified Adams fusion method for the oxygen evolution reaction, Catalysts **9**, 318 (2019).
[28] W.-H. Ryu, Y. W. Lee, Y. S. Nam, D.-Y. Youn, C. B. Park, and I.-D. Kim, Crystalline IrO_2-decorated TiO_2 nanofiber scaffolds for robust and sustainable solar water oxidation, J. Mater. Chem. A **2**, 5610 (2014).
[29] W. W. Pai, T. Y. Wu, C. H. Lin, B. X. Wang, Y. S. Huang, and H. L. Chou, A cross-sectional scanning tunneling microscopy study of IrO_2 rutile single crystals, Surf. Sci. **601**, L69 (2007).
[30] S. Anantharaj, P. E. Karthik, and S. Kundu, Self-assembled IrO_2 nanoparticles on a DNA scaffold with enhanced catalytic and oxygen evolution reaction (OER) activities, J. Mater. Chem. A **3**, 24463 (2015).
[31] K. Guo, Y. Li, T. Yuan, X. Dong, X. Li, and H. Yang, Ultrafine IrO2 nanoparticle-decorated carbon as an electrocatalyst for rechargeable Li-O_2 batteries with enhanced charge performance and cyclability, J. Solid State Electrochem. **19**, 821 (2015).
[32] A. P. Bartók, R. Kondor, and G. Csányi, On representing chemical environments, Phys. Rev. B **87**, 184115 (2013).
[33] P. Giannozzi *et al.*, QUANTUM ESPRESSO: a modular and open-source software project for quantum simulations of materials, J. Phys.: Condens. Matter **21**, 395502 (2009).
[34] B. Hammer, L. B. Hansen, and J. K. Nørskov, Improved adsorption energetics within density-functional theory using revised Perdew-Burke-Ernzerhof functionals, Phys. Rev. B **59**, 7413 (1999).
[35] D. Opalka, C. Scheurer, and K. Reuter, *Ab Initio* thermodynamics insight into the structural evolution of working IrO_2 catalysts in proton-exchange membrane electrolyzers, ACS Catal. **9**, 4944 (2019).
[36] See Supplemental Material at http://link.aps.org/supplemental/10.1103/PhysRevLett.125.206101 for additional details regarding computations and experiments, which also includes Refs. [37–43].
[37] D. R. Hamann, Optimized norm-conserving Vanderbilt pseudopotentials, Phys. Rev. B **88**, 085117 (2013).
[38] K. Reuter and M. Scheffler, Composition, structure, and stability of $RuO_2(110)$ as a function of oxygen pressure, Phys. Rev. B **65**, 035406 (2001).
[39] K. Reuter and M. Scheffler, First-Principles Atomistic Thermodynamics for Oxidation Catalysis: Surface Phase Diagrams and Catalytically Interesting Regions, Phys. Rev. Lett. **90**, 046103 (2003).
[40] M. W. Chase, *NIST-JANAF Thermochemical Tables*, 4th ed. (AIP, New York, 1998), https://dx.doi.org/10.18434/T42S31.
[41] M. Schmid, Chemical potential calculator, http://www.iap.tuwien.ac.at/www/surface/chemical_potentials.
[42] V. Blum, R. Gehrke, F. Hanke, P. Havu, V. Havu, X. Ren, K. Reuter, and M. Scheffler, *Ab initio* molecular simulations with numeric atom-centered orbitals, Comput. Phys. Commun. **180**, 2175 (2009).
[43] V. Pfeifer *et al.*, The electronic structure of iridium oxide electrodes active in water splitting, Phys. Chem. Chem. Phys. **18**, 2292 (2016).

[44] T. Wang, J. Jelic, D. Rosenthal, and K. Reuter, Exploring pretreatment-morphology relationships: ab initio Wulff construction for RuO_2 nanoparticles under oxidising conditions, ChemCatChem **5**, 3398 (2013).

[45] J. P. Perdew, K. Burke, and M. Ernzerhof, Generalized Gradient Approximation Made Simple, Phys. Rev. Lett. **77**, 3865 (1996).

[46] O. Dulub, C. Di Valentin, A. Selloni, and U. Diebold, Structure, defects, and impurities at the rutile $TiO_2(001)$ -(2×1) surface: A scanning tunneling microscopy study, Surf. Sci. **600**, 4407 (2006).

[47] S. J. Freakley, J. Ruiz-Esquius, and D. J. Morgan, The X-ray photoelectron spectra of Ir, IrO_2 and $IrCl_3$ revisited, Surf. Interface Anal. **49**, 794 (2017).

[48] E. Lundgren, G. Kresse, C. Klein, M. Borg, J. N. Andersen, M. De Santis, Y. Gauthier, C. Konvicka, M. Schmid, and P. Varga, Two-Dimensional Oxide on Pd(111), Phys. Rev. Lett. **88**, 246103 (2002).

[49] C. T. Campbell, Transition Metal Oxides: Extra Thermodynamic Stability as Thin Films, Phys. Rev. Lett. **96**, 066106 (2006).

[50] K. Reuter, Nanometer and subnanometer thin oxide films at surfaces of late transition metals, in *Nanocatalysis*, edited by U. Heiz and U. Landman (Springer, Berlin, 2007), p. 343–376, https://doi.org/10.1007/978-3-540-32646-5_5.

[51] All input and output files for the DFT training structures are available at the NOMAD database and can be retrieved under the link https://dx.doi.org/10.17172/NOMAD/2020.08.23-2.